Research Article Vol. 33, No. 3 / 10 Feb 2025 / Optics Express 4926
Optics EXPRESS

Deep-red planar waveguide laser operation of Eu^{3+}:$KY(WO_4)_2$ layers

Amandine Baillard,[1] Ji Eun Bae,[1] Mailyn Ceballos,[2] Pavel Loiko,[1] Rosa Maria Solé,[2] Magdalena Aguiló,[2] Francesc Díaz,[2] Gurvan Brasse,[1] Xavier Mateos,[2] and Patrice Camy[1,*]

[1]*Centre de Recherche sur les Ions, les Matériaux et la Photonique (CIMAP), UMR 6252 CEA-CNRS-ENSICAEN, Université de Caen Normandie, 6 Boulevard Maréchal Juin, 14050 Caen Cedex 4, France*
[2]*Física i Cristal·lografia de Materials (FiCMA), Universitat Rovira i Virgili (URV), 43007 Tarragona, Spain*
[*]*patrice.camy@ensicaen.fr*

Abstract: We report on the first deep-red europium planar waveguide laser. It employs 30-μm thick heavily-doped 11.5 at.% Eu:$KY(WO_4)_2$ layers grown by liquid phase epitaxy on undoped substrates using $K_2W_2O_7$ as a solvent. When pumped with a green laser at 532 nm, the Eu-waveguide laser delivers a maximum output power of 7 mW at 704.7 nm with a slope efficiency of 9.5%, a laser threshold of 21 mW, and linear polarization. The waveguide propagation losses are as low as 0.05 dB/cm. The morphology, vibronic, and spectroscopic properties of the epitaxial layers are also studied. In the deep red, for the $^5D_0 \rightarrow {}^7F_4$ transition, the stimulated-emission cross-section reaches 1.76×10^{-20} cm^2 at 704.7 nm for light polarization $\boldsymbol{E} \parallel N_p$, and the luminescence lifetime of the $^5D_0$ manifold is 472 μs.

1. Introduction

Trivalent europium ions (Eu^{3+}, electronic configuration: [Xe]$4f^6$) are known for their multicolor emissions ranging from yellow to deep-red, due to radiative transitions originating from the metastable state $^5D_0$ to a group of lower-lying manifolds ^7F_J ($J = 0 - 6$, $^7F_0$ being the ground state), Fig. 1. Owing to a large energy-gap between the $^5D_0$ state and the next lower-lying level $^7F_6$ (about 12000cm^{-1}), no depopulation of the emitting state occurs by multiphonon non-radiative relaxation, even in high-phonon energy matrices. Eu^{3+}-doped materials do not suffer from self-quenching via cross-relaxation enabling high available doping concentrations [1]. Usually, the red emission at 613 nm (the electric dipole $^5D_0 \rightarrow {}^7F_2$ transition) dominates in the spectra of Eu^{3+}-doped materials (*i.e.*, it corresponds to the highest luminescence branching ratio) paving the way towards high color purity luminophores (phosphors) [2]. In addition, the presence of a purely magnetic dipole $^5D_0 \rightarrow {}^7F_1$ transition at 591 nm, whose probability is almost independent of the host matrix, enables the use of Eu^{3+} ions as structural probes: the intensity ratio between the "hypersensitive" $^5D_0 \rightarrow {}^7F_2$ transition and the $^5D_0 \rightarrow {}^7F_1$ one is often calculated to evaluate the site symmetry where Eu^{3+} is residing [3]. Recently, Eu^{3+} ions attracted a lot of attention for the development of quantum technologies, in particular for their unusually long coherence lifetimes and ultra-narrow optical homogeneous linewidths [4,5].

Moreover, Eu^{3+} ions are suitable for the development of visible lasers emitting in the red and deep red. Despite a recent breakthrough in rare-earth ion-based lasers directly emitting in the visible under pumping in the blue [6], there exist very few studies on Eu visible lasers. This is probably due to the extremely narrow and weak absorption lines of Eu^{3+} (due to the

#537598 https://doi.org/10.1364/OE.537598
Journal © 2025 Received 25 Jul 2024; revised 4 Nov 2024; accepted 10 Nov 2024; published 31 Jan 2025

Optics EXPRESS

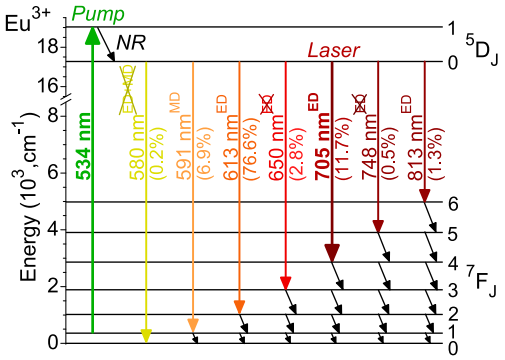

Fig. 1. Partial energy-level scheme of Eu^{3+} ions (after Carnall *et al.* [11]). *Arrows* – transitions in absorption and emission, NR – multiphonon non-radiative relaxation, ED and MD – electric and magnetic dipole transitions, respectively (*crosses* indicate transitions forbidden by selection rules), *numbers in parentheses* – luminescence branching ratios, *B*(JJ').

spin-forbidden nature of the corresponding transitions, $\Delta S \neq 0$), imposing serious requirements on the pump sources. The first room-temperature solid-state Eu laser was demonstrated in 2004 by Park and Steckl, using 1-3 at.% Eu^{3+}:GaN semiconductor thin films grown by molecular beam epitaxy on sapphire substrates. The 0.6-µm-thick films were optically pumped by a UV nitrogen gas laser emitting at 337 nm, achieving stimulated emission in the red, at 620 nm [7]. This result also represents the first Eu waveguide laser action. Further progress in bulk Eu lasers was achieved implementing double tungstate crystals heavily doped with Eu^{3+} (25 at.%) [8,9]. Finally, a breakthrough was achieved in 2021 with a stoichiometric $KEu(WO_4)_2$ compound, delivering Watt-level output power at 703 nm (in the deep-red) with a slope efficiency of 43.2%, a low laser threshold of 64 mW and a linearly polarized emission [10].

Red and deep-red laser sources are extensively employed in our daily life, for example in display technologies [12] and optical data storage [13], but also in cutting-edge applications such as medicine, fluorescence microscopy or contactless sensing. In medicine, red and deep-red lasers are of great interest for the photochemical activation of specific drugs and substances [14]. As red light offers deep penetration into bio-tissues, red lasers have found their niche in dermatology [15]. Red lasers are also relevant for stimulated-emission-depletion microscopy, allowing to overcome the limit of resolution imposed by diffraction of light [16]. The laser-based interface measurement technique is using red lasers to measure concentration and temperature variations in liquids, at transparent interfaces between liquids and solids. These measurements are essential for microfluidic, studies of heat transfer and mass diffusion, and micro-electro-mechanical systems [17]. Red light irradiation is also found in agriculture for biostimulation purposes [18].

The crystal family of monoclinic potassium rare-earth double tungstates $KR(WO_4)_2$ (R = Y, Lu, Gd) has been extensively studied for doping with trivalent rare-earth ions for near-infrared lasers [19–21]. These materials combine several advantages, *i.e.*, i) very high transition cross-sections for polarized light, ii) high available rare-earth doping levels up to stoichiometric compositions, iii) weak concentration quenching of luminescence due to the large interatomic distances, iv) Raman activity, and v) reasonable thermal and thermo-optical properties. Recently, there is raising interest in visible lasers employing monoclinic double tungstates doped with Dy^{3+} [22], Eu^{3+} [8,9] and Sm^{3+} [23,24] ions.

Waveguide lasers represent an important component of integrated photonic circuits. They are compatible with optical fibers and on-chip devices leading to applications in optical sensing, on-chip spectroscopy, and microfluidics. This laser architecture benefits from small mode areas

Optics EXPRESS

leading to high intracavity light intensities, low laser thresholds, good spatial beam quality and high efficiency [25,26].

This paper reports on a deep-red planar waveguide laser based on Eu^{3+}-doped monoclinic double tungstate epitaxial layers grown by Liquid Phase Epitaxy (LPE). The LPE technique is well suited for elaboration of single-crystalline oriented layers of high optical quality (with propagation losses down to 0.1 dB/cm [27]), even for strongly anisotropic materials like double tungstates. Growth, spectroscopy and laser action in the near-infrared spectral range (1–2 µm) of $KR(WO_4)_2$ epitaxial layers doped with Yb^{3+}, Tm^{3+} and Ho^{3+} ions were reported [28–30].

There exist studies on fabrication of Eu^{3+}-doped luminescent crystalline layers of various compositions. In general, Eu^{3+}-doped garnets have been fabricated by LPE for scintillators [31,32], while epitaxial layers of $Eu_3Ga_5O_{12}$ were also studied for optical waveguides [33]. Other physical and chemical methods are also available for the growth of films doped with Eu^{3+} ions, such as sol-gel [34], atomic layer deposition [35], chemical vapour deposition [36], sputtering [37], metal organic vapour phase epitaxy with ion implantation [38], matrix-assisted pulsed laser evaporation technique [39], spray pyrolysis [40], pulsed laser deposition [41], electrodeposition [42], or chemical-bath deposition [43]. Nevertheless, none of these Eu^{3+}-doped layers were involved in planar waveguide laser experiments.

2. Liquid phase epitaxy growth

Eu^{3+}-doped $KY(WO_4)_2$ layers were grown on undoped bulk $KY(WO_4)_2$ substrates by the Liquid Phase Epitaxy method using potassium ditungstate $K_2W_2O_7$ as a solvent in air atmosphere. The solute to solvent ratio was 7 mol% $KY_{0.90}Eu_{0.10}(WO_4)_2$–93 mol% $K_2W_2O_7$. The bulk crystals used for the substrate preparation were grown by the Top-Seeded Solution Growth (TSSG) method. The substrates with dimensions of 8×22 mm^2 (width × length ($||\boldsymbol{c}$ crystallographic direction)) and a thickness of 2 mm were cut with their plane orthogonal to the [010] crystallographic axis. They were polished to laser-grade quality from both sides (surface roughness: < 1 nm) and thoroughly cleaned before the epitaxial growth. After carefully determining the saturation temperature of the solution, the substrates were slowly introduced in the furnace to avoid thermal shocks. The substrates were first heated for 1 h above the solution surface and then dipped vertically several millimeters in the solution at a temperature 1 °C higher than the saturation temperature for 5 min, to dissolve slightly the outer part of the substrate. The growth was performed by slow cooling of 4 °C from the saturation temperature (845 °C) at a rate of 0.2 °C/h and rotating the substrate at 10 rpm resulting in a layer thickness of ∼100 µm (on both sides of the substrate). The growth duration was 20 h, and the epitaxial growth rate was around 9.5 mg/h. After the growth, the epitaxy was removed from the flux and slowly cooled down to room temperature to prevent any thermal stress that could produce cracks. No additional cladding layer was deposited. Figure 2(a,b) depicts the photographs of the as-grown epitaxy, both under natural light and UV illumination. The layers are transparent and nearly colorless. When exposed to a UV lamp, they emit bright orange-red luminescence due to Eu^{3+} ions.

For laser experiments, the top surface of the epitaxy was polished to laser-grade quality reducing the layer thickness down to 30 ± 1 µm, as well as the two side facets, resulting in a length ℓ of 8.37 mm.

The actual Eu^{3+} doping level in the layers was determined from the polarized absorption spectra and absorption cross-sections measured independently from a reference stoichiometric $KEu(WO_4)_2$ crystal. This analysis yielded 11.5 at.% Eu (ion density: $N_{Eu} = 7.3 \times 10^{20}$ at/cm^3) and a segregation coefficient $K_{Eu} = C_{layer}/C_{solution}$ of 1.15. The Eu^{3+} ions are substituting Y^{3+} ones in a single type of sites with C_2 symmetry. Their ionic radii are $R_{Eu} = 1.066$ Å and $R_Y = 1.019$ Å for VIII-fold oxygen coordination [45].

Undoped $KY(WO_4)_2$ crystals are monoclinic (space group $C^6_{2h} - C2/c$). They are optically biaxial, and their optical properties are described within the optical indicatrix frame {N_p, N_m,

Optics EXPRESS

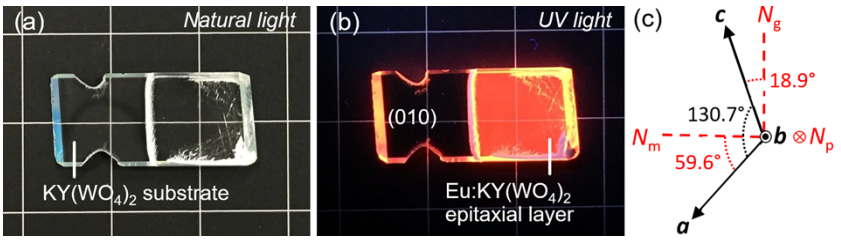

Fig. 2. (a,b) Photographs of the as-grown 11.5 at.% Eu:$KY(WO_4)_2$ epitaxy: (a) in natural light, (b) under UV illumination; (c) orientation of the optical indicatrix frame $\{N_p, N_m, N_g\}$ with respect to the crystallographic axes $\{\boldsymbol{a}, \boldsymbol{b}, \boldsymbol{c}\}$ using the standard $C2/c$ setting reported in [44].

$N_g\}$, corresponding to the principal axes of the index ellipsoid, which are labelled following the convention $n_p < n_m < n_g$. The orientation of the optical indicatrix frame with respect to the crystallographic axes is depicted in Fig. 2(c) at the wavelength of 633 nm (in the red, note the apparent rotation of the dielectric frame with the wavelength) [44]. The N_p-axis is parallel to the $\boldsymbol{b}$ crystallographic axis which is the 2-fold symmetry axis (C_2), and N_m and N_g ones lie in the $\boldsymbol{a}$-$\boldsymbol{c}$ mirror plane (m) [19]. The angle between the N_m and $\boldsymbol{a}$ axes is 59.6° (within the monoclinic angle $\beta = \boldsymbol{a}\hat{\boldsymbol{c}}$) and the one between the N_g and $\boldsymbol{c}$ axis is 18.9° (out of the monoclinic angle). Therefore, the absorption and emission properties of Eu^{3+} ions were studied for the principal light polarizations $\boldsymbol{E} \parallel N_p$, $\boldsymbol{E} \parallel N_m$, $\boldsymbol{E} \parallel N_g$ (note that it was predicted that for monoclinic crystals, the eigen frames of absorption / emission may not necessarily coincide with that of the optical indicatrix [46]).

The principal refractive indices of both the undoped substrate and the Eu^{3+}-doped epitaxial layer were measured using a prism-film coupler (Metricon 2010) equipped with a He-Ne laser at 632.8 nm. The results are listed in Table 1. The refractive indices of the substrate are in line with the previously reported values for $KY(WO_4)_2$ [22]. All three principal refractive indices of the epitaxial layer increase upon substituting Y^{3+} by Eu^{3+}. For the light polarization $\boldsymbol{E} \parallel N_p$ (the laser polarization for the developed waveguide), the refractive index contrast $\Delta n = n_{layer} - n_{substrate} = 2.5 \times 10^{-3}$.

Table 1. Measured refractive indices of the $KY(WO_4)_2$ substrate and the Eu^{3+}-doped $KY(WO_4)_2$ epitaxial layer at 632.8 nm.

Material	n_p	n_m	n_g
$KY(WO_4)_2$ substrate	1.9977	2.0405	2.0851
$KY_{0.885}Eu_{0.115}(WO_4)_2$ layer	2.0002	2.0419	2.0853

3. Results and discussion

3.1. Layer morphology, composition and structure

The layer morphology was observed by confocal laser microscopy, Fig. 3. The as-grown surface shown in Fig. 3(b) exhibits growth steps typical of double tungstates elaborated by LPE, with no residual solvent. This behavior can be explained by the growth mechanism (layer by layer), good wettability of the solvent on the substrate surface, and orientation of the substrate. The top surface was further examined in the interferometric mode, and a surface roughness plot revealed very flat terraces with growth steps of about 0.5 µm in height, Fig. 3(c,d). The top and side surfaces of the epitaxy were then polished to laser-grade quality, reducing the layer thickness down to about 30 µm. The epitaxial layer is single crystalline, uniform and free of defects, cracks and

Optics EXPRESS

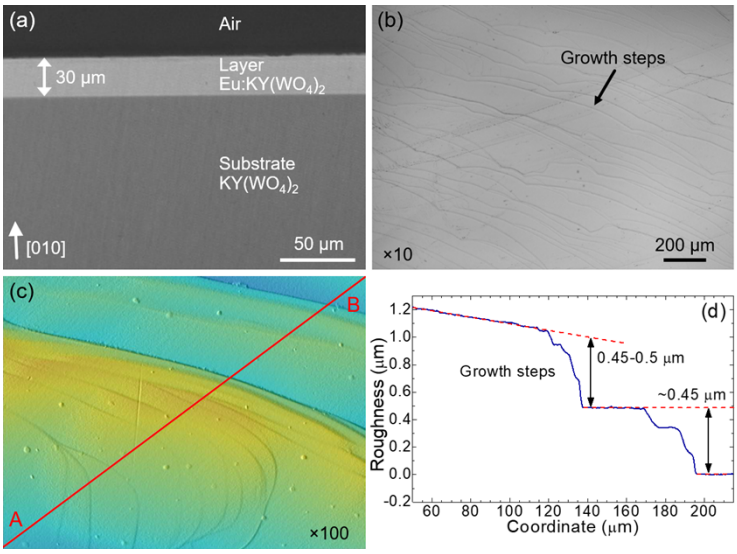

Fig. 3. Observation of the Eu:$KY(WO_4)_2$ epitaxial layers by confocal laser microscopy: (a) side view on the polished end-facet; (b) top view of the as-grown surface; (c) topography of the as-grown surface highlighting the growth steps typical of the LPE growth of double tungstate layers; (d) surface roughness plot along the A–B red line. Reflection mode, $\lambda = 405$ nm.

inclusions, and the interface between the layer and the substrate is clean and distinct, Fig. 3(a). After polishing to laser-grade quality, the parallelism of the faces was better than 15', and the right angle between the top and the output facet was 90° with an accuracy of 30 arcsec.

The composition of the epitaxial layer, as well as the homogeneous distribution of the constituting elements were studied by Energy Dispersive X-ray (EDX) spectroscopy associated with the field emission scanning electron microscopy (FESEM) technique, Fig. 4. This analysis indicated a partial substitution of Y^{3+} by Eu^{3+} within the layer, as well as a homogeneous distribution of the Eu^{3+} dopant (the weak signal of Eu^{3+} from the substrate is due to the noise from the detector).

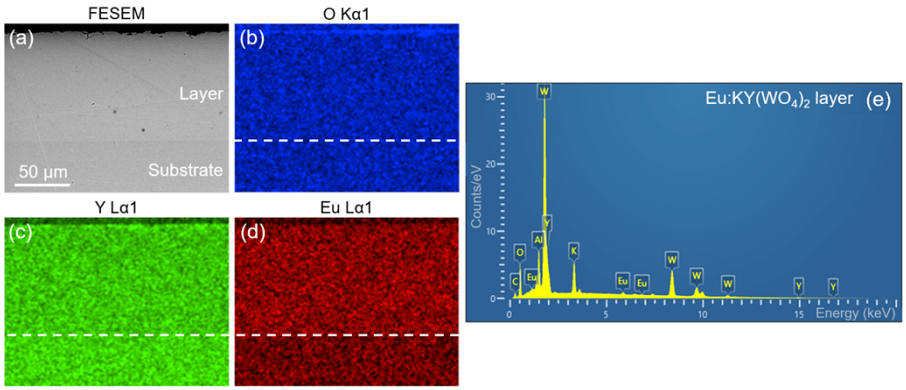

Fig. 4. Energy dispersive X-ray (EDX) based elemental mapping over an end-facet of the Eu:$KY(WO_4)_2$ epitaxial layer: (a-d) element maps: (a) a FESEM image, (b) O Kα1, (c) Y Lα1, (d) Eu Lα1; (e) EDX spectrum of the Eu-doped layer.

Optics EXPRESS

The polarized Raman spectra of the 11.5 at.% Eu:$KY(WO_4)_2$ epitaxial layer are displayed in Fig. 5(a). The measurements were performed in the $\boldsymbol{p}(ij)\bar{\boldsymbol{p}}$ geometry (where $i, j = m, g$) using Porto's notation for polarized Raman spectroscopy [47]. The factor group analysis predicts the following set of irreducible representations at the center of the Brillouin zone $\Gamma(\boldsymbol{k} = 0)$ for monoclinic double tungstates: $17A_g + 19B_g + 17\ Au + 19B_u$, with 36 even (*gerade*) modes, $A_g + B_g$, being Raman active. The assignment of the Raman peaks was done according to the results reported in [48,49]. The phonons having energies below 250 cm^{-1} are associated with translation motions (T) of the cations inside the crystalline structure (namely, K^+, W^{6+}, and $Y^{3+}|Eu^{3+}$). The in- (δ) and out-of-plane (γ) bending modes are found below 380 cm^{-1}. Finally, stretching modes (ν) are located between 400 cm^{-1} and 915 cm^{-1}, with the peaks in the range from 430 cm^{-1} to 750 cm^{-1} corresponding to vibrations of oxygen bridges in compounds where tungsten appears in a V- or VI-fold oxygen coordination (for the studied crystal, these are $[WO_6]$ polyhedra). The highest-energy modes are observed at 903 cm^{-1} and 917 cm^{-1}, with the first one attributed to stretching vibrations within the $[WO_6]$ polyhedra [49].

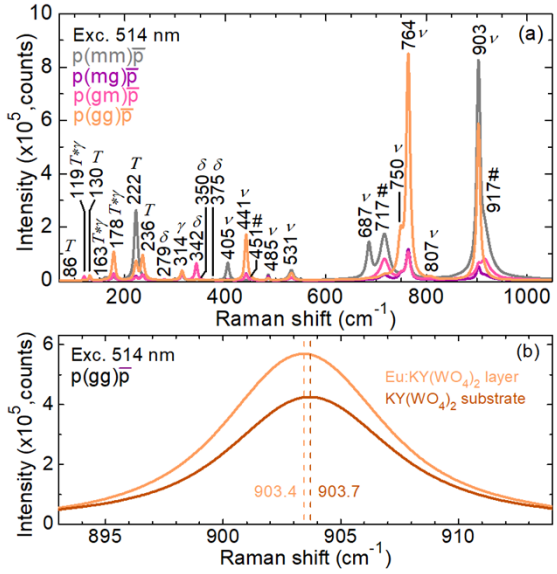

Fig. 5. (a) Polarized μ-Raman spectra of Eu:$KY(WO_4)_2$ epitaxial layer in the $\boldsymbol{p}(ij)\bar{\boldsymbol{p}}$ geometry ($i, j = m, g$); (b) a close look at the Raman peak at 903 cm^{-1} for the epitaxial layer and the undoped substrate in the $\boldsymbol{p}(gg)\bar{\boldsymbol{p}}$ geometry, $\lambda_{exc} = 514$ nm. *Numbers* – Raman frequencies in cm^{-1}, ν – stretching modes, δ and γ – in-plane and out-of-plane bending modes, T – translational modes, * – coupling of different modes, # – modes not assigned.

A comparison was made between the intense Raman peak located at 903 cm^{-1} for both the epitaxial layer and the undoped substrate, Fig. 5(b). A slight red shift of 0.3 cm^{-1} manifests the incorporation of Eu^{3+} ions substituting Y^{3+} ones, thus inducing a small variation of the crystalline structure.

3.2. Optical spectroscopy

Prior to laser experiments, we studied polarized absorption and emission properties of Eu^{3+} ions in the grown epitaxial layers. The absorption cross-sections, $\sigma_{abs} = \alpha_{abs}/N_{Eu}$ (α_{abs} – absorption coefficient), of Eu^{3+} in the blue-green spectral range are plotted in Fig. 6 for the two available light polarizations, $\boldsymbol{E} \parallel N_m$ and N_g. Eu^{3+} presents a strong anisotropy of absorption properties, with the highest cross-sections for light polarized along the N_m-axis. Within the studied spectral

Optics EXPRESS

range, the absorption transitions originate from the ground-state $^7F_0$ and the thermally populated lower-lying excited-state $^7F_1$ and terminate at the $^5D_1$, $^5D_2$, $^5D_3$ and $^5L_6$ higher-lying manifolds. Due to the spin-forbidden nature of these transitions ($\Delta S \neq 0$), they are relatively weak. The weak electron-phonon coupling inherent for Eu^{3+} results in rather narrow absorption linewidths (typically below 1 nm), setting a strong constraint for the choice of the pump wavelength and laser linewidth. Fortunately, due to the lack of cross-relaxation processes among Eu^{3+} ions, it can be leveraged by using heavily doped materials. The pump sources envisioned for Eu lasers are blue (465 nm) GaN-based laser diodes and green (532 nm) frequency-doubled optically pumped semiconductor lasers (2ω-OPSL).

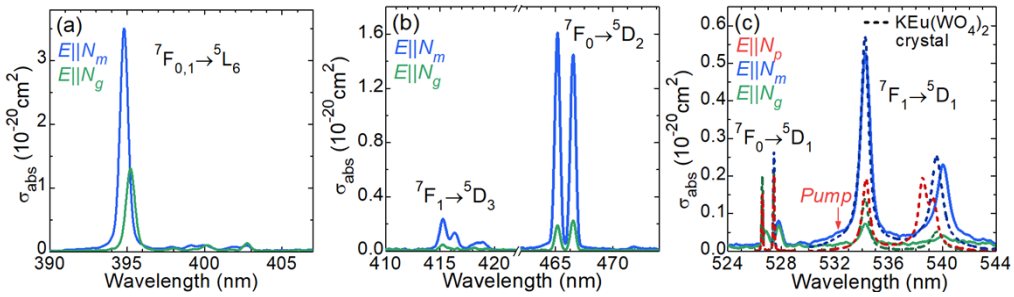

Fig. 6. (a-c) Polarized absorption cross-section, σ_{abs}, spectra of Eu^{3+} ions in the 11.5 at.% Eu:$KY(WO_4)_2$ epitaxial layer for light polarizations $\boldsymbol{E} \parallel N_m$ and N_g. In (c), the spectra for a stoichiometric $KEu(WO_4)_2$ crystal are added for comparison (*dashed lines*). The *arrow* in (c) indicates the pump wavelength.

The $^7F_{0,1} \rightarrow {}^5L_6$ transition corresponds to the highest absorption cross-section of 3.51×10^{-20} cm^2 at 394.8 nm for light polarization $\boldsymbol{E} \parallel N_m$, Fig. 6(a). For the $^7F_0 \rightarrow {}^5D_2$ absorption band which can be addressed by 465-nm GaN laser diodes, two intense absorption peaks are found at 465.2 nm and 466.5 nm, with σ_{abs} of 1.61×10^{-20} cm^2 and 1.45×10^{-20} cm^2, respectively, also for $\boldsymbol{E} \parallel N_m$, Fig. 6(b). The $^7F_1 \rightarrow {}^5D_1$ transition falling in the green exhibits lower cross-sections, $\sigma_{abs} = 0.53 \times 10^{-20}$ cm^2 at 534.3 nm (absorption linewidth: 0.9 nm) again for $\boldsymbol{E} \parallel N_m$, Fig. 6(c). In the latter figure, the spectra measured for the $KEu(WO_4)_2$ crystal are shown for comparison, adding the light polarization $\boldsymbol{E} \parallel N_p$ inaccessible for epitaxial layers.

The pump source employed in the present study was a continuous-wave (CW) solid-state laser emitting in the green (at 532.2 nm), thus falling on the side (phonon sideband) of the $^7F_1 \rightarrow {}^5D_1$ absorption band (so called "wing-pumping"). The pump polarization corresponded to $\boldsymbol{E_p} \parallel N_p$ (in the layer), and the corresponding absorption cross-section σ_{abs} was only 0.7×10^{-22} cm^2 (measured for the $KEu(WO_4)_2$ crystal).

The polarized luminescence spectra of Eu:$KY(WO_4)_2$ epitaxy in the visible spectral range are shown in Fig. 7(a). Eu^{3+} ions exhibit strong anisotropy of emission properties which is a prerequisite for linearly polarized laser emission. The most intense emission corresponds to the $^5D_0 \rightarrow {}^7F_2$ transition in the red. The stimulated-emission (SE) cross-sections, σ_{SE}, for the $^5D_0 \rightarrow {}^7F_2$ and $^7F_4$ transitions were calculated via the Füchtbauer-Ladenburg formula [50]:

$$\sigma_{SE}^{i}(\lambda) = \frac{\lambda^5}{8\pi c \langle n \rangle^2 \tau_{rad}} \times \frac{B(JJ')W_i(\lambda)}{\frac{1}{3}\sum_{j=p,m,g} \int \lambda W_j(\lambda) d\lambda}, \quad (1)$$

where λ is the light wavelength, c is the speed of light, $<n>$ is the mean refractive index of the host matrix at the emission wavelength, τ_{rad} is the radiative lifetime of the emitting state ($^5D_0$), $W_i(\lambda)$ is the measured luminescence spectrum for the i-th polarization ($i = p, m, g$), and B(JJ') is the luminescence branching ratio. The results are displayed in Fig. 7(b,c).

Optics EXPRESS

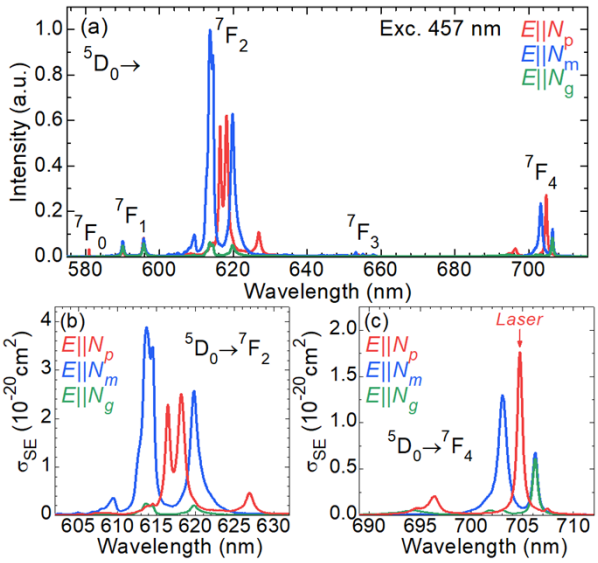

Fig. 7. Polarized emission properties of Eu^{3+} ions in the 11.5 at.% Eu:$KY(WO_4)_2$ epitaxial layer: (a) luminescence spectra, $\lambda_{exc} = 457$ nm; (b,c) stimulated-emission cross-sections, σ_{SE}: (b) the $^5D_0 \rightarrow {}^7F_2$ transition in the red, (c) the $^5D_0 \rightarrow {}^7F_4$ transition in the deep-red. The light polarizations are $\boldsymbol{E}$ || N_p, N_m, and N_g. The *arrow* in (c) indicates the laser wavelength.

In the red, for the $^5D_0 \rightarrow {}^7F_2$ transition, the maximum σ_{SE} is 3.89×10^{-20} cm^2 at 613.7 nm for light polarization $\boldsymbol{E}$ || N_m (experimental luminescence branching ratio: $B(0\rightarrow2) = 76.6\%$). In the deep-red, for the $^5D_0 \rightarrow {}^7F_4$ transition, the peak σ_{SE} is smaller, measuring 1.76×10^{-20} cm^2 at 704.7 nm for $\boldsymbol{E}$ || N_p ($B(0\rightarrow4) = 11.7\%$), corresponding to an emission linewidth of 0.6 nm. The luminescence branching ratios of each Eu^{3+} radiative transition in the $KY(WO_4)_2$ epitaxial layer are given in Fig. 1. The near-infrared emissions due to transitions $^5D_0 \rightarrow {}^7F_5$ and $^5D_0 \rightarrow {}^7F_6$ are not included in Fig. 7(a) due to their low intensity (the corresponding luminescence branching ratios are $B(0\rightarrow5) = 0.5\%$ and $B(0\rightarrow6) = 1.3\%$).

The luminescence decay from the $^5D_0$ emitting state of Eu^{3+} ions in the epitaxial layer was studied by monitoring the red luminescence at 610 nm and exciting the active ions at 395 nm, Fig. 8. The decay curve for the stoichiometric $KEu(WO_4)_2$ crystal was added for comparison. The measured luminescence lifetime τ_{lum} amounted to 472 µs for the epitaxial layer, being only slightly shorter than that for the single crystal (479 µs). It is also close to the radiative lifetime ($\tau_{rad} = 464$ µs) calculated using the Judd-Ofelt theory in a previous work [2] thus indicating a luminescence quantum efficiency close to unity. This highlights the high optical quality and crystallinity of the layer being free of quenching centers such as defects and impurities. The decay curves are single exponential, in agreement with the single type of sites (C_2 symmetry) for Eu^{3+} ions in $KY(WO_4)_2$ crystals.

The homogeneity of the layer, including the homogeneity of distribution of active ions, was confirmed by μ-luminescence and μ-Raman mapping performed across the polished end-facet of the Eu:$KY(WO_4)_2$ / $KY(WO_4)_2$ epitaxy, Fig. 9. The Eu^{3+} ions are uniformly distributed in the layer and no diffusion into the substrate can be observed. The μ-Raman mapping confirms the slight modification of the material structure due to the heavy Eu^{3+} doping.

Optics EXPRESS

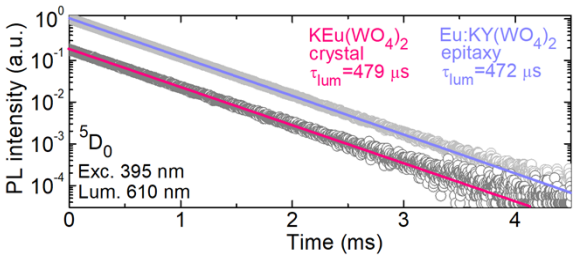

Fig. 8. Luminescence decay curve from the $^5D_0$ emitting state of Eu^{3+} in the 11.5 at.% Eu:$KY(WO_4)_2$ epitaxial layer, *circles* – experimental data, *line* – their exponential fit, $\lambda_{exc} = 395$ nm, $\lambda_{lum} = 610$ nm. The decay curve for a $KEu(WO_4)_2$ bulk crystal is added for comparison.

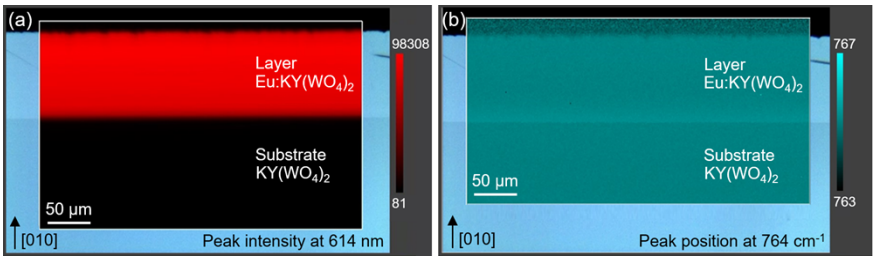

Fig. 9. Mapping across the polished end-facet of the Eu:$KY(WO_4)_2$ / $KY(WO_4)_2$ epitaxy: (a) μ-luminescence mapping monitoring the peak intensity at 614 nm (the $^5D_0 \rightarrow {}^7F_2$ transition); (b) μ-Raman mapping monitoring the peak position at 764 cm^{-1}, in the $\boldsymbol{p}(gm)\bar{\boldsymbol{p}}$ geometry.

3.3. *Planar waveguide laser*

The layout of the laser set-up, as well as a photograph of the laser cavity are depicted in Fig. 10. The pump source was a commercial CW green solid-state laser delivering multi-Watt output at 532.2 nm (laser linewidth: 0.15 nm) with linear polarization and almost diffraction-limited beam (measured beam quality factor $M^2 = 1.02$), addressing the $^7F_1 \rightarrow {}^5D_1$ absorption band of Eu^{3+} ions. The pump polarization was adjusted using an anti-reflection (AR) coated half-wave plate corresponding to $\boldsymbol{E}_\mathbf{p} \parallel N_p$ (vertical) in the waveguide. The pump radiation was coupled into the layer using an AR coated achromatic lens (focal length: $f = 60$ mm). The linear laser cavity was formed by a plane pump mirror (PM) coated for high transmission (HT, $T > 97.0\%$) at 532 nm and high reflection (HR, $R > 99.8\%$) at 705 nm, and a set of plane output couplers (OCs) with a transmission T_{OC} ranging from 0.3% to 3.0% at the laser wavelength. Both bulk cavity mirrors were slightly pressed towards the waveguide end-facets, consequently forming a compact quasi-monolithic cavity. No index-matching fluid was used. The epitaxy was mounted on a Cu-holder using a silver paint for better heat removal. The waveguide length ℓ was 8.37 mm, and it was oriented for light propagation along the N_m-axis (N_m-cut). A mechanical chopper was implemented to modulate the pump beam (duty cycle: 1:12, pump pulse duration: 40 ms) to avoid detrimental thermal effects. Below, we will refer to this as quasi-CW excitation. The residual pump after the OC was filtered out using a long-pass filter (FELH0650, Thorlabs). The single-pass pump absorption was relatively low (3.1%) as the pump source enabled wing-pumping.

The laser emission spectra were measured using an optical spectrum analyzer (Yokogawa, AQ6373). The oscilloscope traces of laser emission were captured using a fast photodiode and an 8 GHz digital oscilloscope (DSA70804B, Tektronix), under quasi-CW excitation. The spatial profiles of the pump and laser modes, as well as the guided luminescence in the near field were

Optics EXPRESS

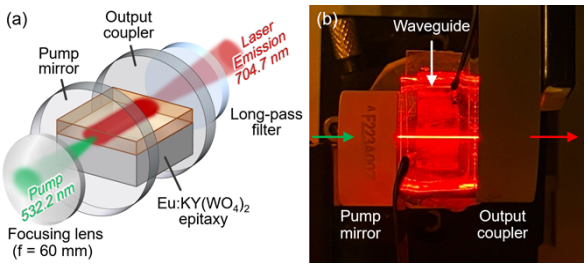

Fig. 10. Planar Eu waveguide laser: (a) scheme of the laser set-up, (b) a photograph of the laser cavity.

taken using a short focal length ($f = 15$ mm) spherical uncoated CaF_2 lens (Thorlabs) and a CCD camera (BladeCam2-XHR, DataRay). For scale calibration, the waveguide with a known thickness was illuminated using a white light source. The input-output dependencies were also measured under quasi-CW excitation.

The power characterization of the developed laser is shown in Fig. 11(a). The deep-red planar waveguide laser generated a maximum output power of 7 mW at 704.7 nm with a slope efficiency η of 9.5% (vs. the absorbed pump power) and a very low laser threshold P_{th} of 21 mW, when using 1.3% output coupling. On decreasing the transmission of the output coupler, the threshold gradually decreased from 23 mW ($T_{\mathrm{OC}} = 3.0\%$) to 14 mW ($T_{\mathrm{OC}} = 0.3\%$). Such a low-threshold behavior is related to the four-level scheme of the Eu laser without reabsorption, a relatively long luminescence lifetime of the upper laser level ($^5D_0$), and a small laser mode area. The laser emission was linear polarized ($\boldsymbol{E}_{\mathbf{L}} \parallel N_{\mathrm{p}}$), and the polarization state was naturally selected by the anisotropy of the emission, Fig. 7(c). A typical spectrum of laser emission for $T_{\mathrm{OC}} = 1.0\%$ is given in Fig. 11(b) and compared with the fluorescence spectrum for the respective light polarization. The laser emission spectrum was relatively broad, and its multi-line structure was determined by the etalon (Fabry-Perot) effects at the crystal / mirror interfaces (laser linewidth: ~0.6 nm). A typical oscilloscope trace of laser emission measured under quasi-CW excitation reveals a spiking behavior, see Fig. 11(c).

The Findlay-Clay analysis was applied to evaluate the waveguide propagation losses [51], as shown in Fig. 11(d). The following formula links the laser threshold P_{th} and the output coupler reflectivity, $R_{\mathrm{OC}} = 1 - T_{\mathrm{OC}}$:

$$-\ln(R_{OC}) = 2KP_{th} - L, \tag{2}$$

where K is a constant, and L is the roundtrip passive loss corresponding to the y-intercept of the linear fit. This analysis yields $L = 1.8 \pm 0.5\%$, giving an upper estimate for the waveguide propagation loss $\delta_{\mathrm{loss}} = 4.34\, L/(2\ell)$ of 0.05 dB/cm.

The near-field modal profiles of the guided green pump radiation, red luminescence and deep-red laser emission are shown in Fig. 12. Both the pump and laser modes are well confined within the epitaxial layer, see Fig. 12(a,c). The photographs of the red luminescence and deep-red laser beam are also given as insets in Fig. 12(b) and (c), respectively. They exhibit a stripe-like shape typical for planar waveguides with light confinement in only one direction (vertical).

The 1D intensity profiles of the laser mode are displayed in Fig. 12(d). The intensity profile is reasonably well fitted with a Gaussian distribution in the horizontal direction (*i.e.*, in the waveguide plane) yielding a mode diameter (at the $1/e^2$ level) of 179 µm, and, as expected due to the lack of cladding, the intensity profile is strongly asymmetric in the vertical direction (beam diameter: 16 µm). According to the measured refractive index contrast, the waveguide is strongly multimode in the latter direction.

Eu^{3+} ions exhibit their most intense emission in the red, at 613 nm. However, it was proven difficult to achieve room temperature lasing in this spectral range [1,52]. This could be explained

Optics EXPRESS

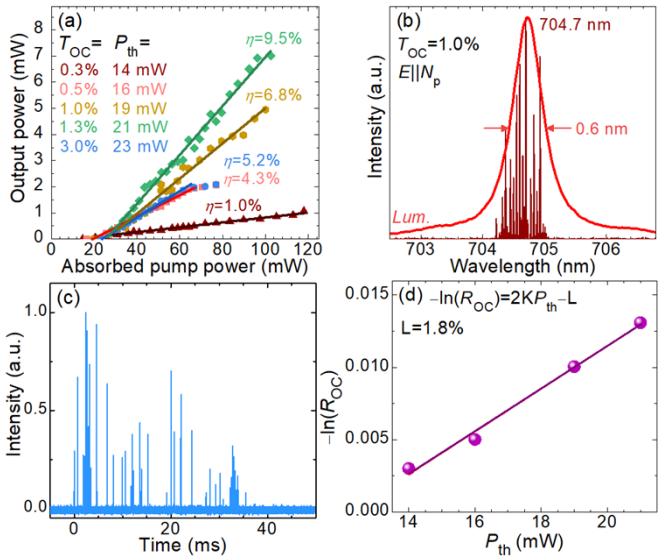

Fig. 11. Eu:KY$(WO_4)_2$ deep-red planar waveguide laser: (a) input-output dependences under quasi-CW excitation, η – slope efficiency, P_{th} – laser threshold; (b) a typical laser spectrum, T_{OC} = 1.0%, *red curve* – luminescence spectrum (for both, the polarization state is $\boldsymbol{E}$ || N_p); (c) a typical oscilloscope trace of laser emission under quasi-CW excitation; (d) estimation of the roundtrip passive loss L via the Findlay-Clay analysis.

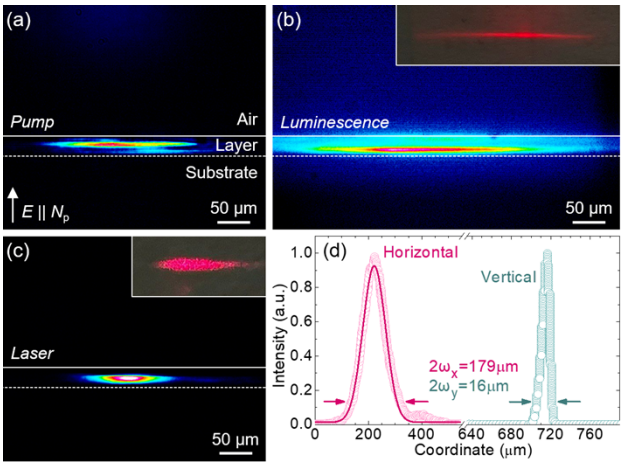

Fig. 12. Modal behavior of the Eu:KY$(WO_4)_2$ planar waveguide: (a-c) near field mode profiles: (a) guided pump at 532 nm ($\boldsymbol{E_P}$ || N_p), (b) guided luminescence at 613 nm (unpolarized), (c) laser mode at 705 nm ($\boldsymbol{E_L}$ || N_p). *White lines* – the air / layer and layer / substrate interfaces. The *insets* show photographs of (b) the red luminescence in the far-field and (c) the deep-red laser beam; (d) 1D intensity profiles of the laser mode in the horizontal and vertical directions, s*ymbols* – experimental data, *curve* – Gaussian fit.

Optics EXPRESS

by resonant excited-state absorption processes originating from the upper laser level ($^5D_0$) to higher-lying 4f manifolds, and / or reabsorption from the thermally populated terminal laser level ($^7F_2$). Stimulated emission of Eu^{3+} ions in the red was only observed at cryogenic temperatures owing to the decreased thermal population of the $^7F_2$ manifold [53,54].

4. Conclusions

To conclude, we report on the first Liquid Phase Epitaxy growth of $KY(WO_4)_2$ layers heavily doped (11.5 at.%) with Eu^{3+} ions, as well as the first deep-red Eu waveguide laser employing a dielectric material as gain medium. The grown epitaxial layers feature i) a well-preserved orientation, ii) a uniform distribution of the dopant ions with no migration into the substrate, iii) a strong polarization of emission properties of Eu^{3+} ions in the red and deep-red giving rise to linear laser polarization, iv) a relatively long upper laser level luminescence lifetime and almost no quenching via energy migration to defects and impurities, and v) low waveguide propagation losses (0.05 dB/cm) in the deep-red. Altogether, this makes Eu:$KY(WO_4)_2$ layers a promising platform for compact, low threshold visible laser sources.

Further power scaling and improvement of the laser efficiency is expected by boosting the pump absorption in the layers, namely via their proper orientation to access the desired light polarization $\boldsymbol{E} \parallel N_m$ with the highest absorption cross-sections, as well as increasing the Eu^{3+} content in the layers potentially up to the stoichiometric composition. Diode-pumping of such waveguides could be another solution, *e.g.*, when using 465 nm GaN-based blue laser diodes addressing the $^7F_0 \rightarrow {}^5D_2$ absorption band. The microstructuring of grown layers by means of precision diamond saw dicing could lead to fabrication of surface channel (ridge) waveguides with yet lower laser thresholds and improved slope efficiencies owing to the smaller mode areas and better overlap between the pump and laser modes.

Funding. Région Normandie, France (Contrat de plan État-Région (CPER), Programme WINNINGNormandy); Agence Nationale de la Recherche (ANR-22-CE08-0025-01, NOVELA, ANR-23-LCV2-0001-01, LOVINOV); Project PID2022-141499OB-100 funded by MICIU/AEI/10.13039/501100011033/ and by FEDER/UE; H2020 Marie Skłodowska-Curie Actions (101034329).

Acknowledgments. Xavier Mateos is a Serra Húnter Fellow with the Serra Húnter Programme, Catalan University, Spain.

Disclosures. The authors declare no conflicts of interest.

Data availability. Data underlying the results presented in this paper are not publicly available at this time but may be obtained from the authors upon reasonable request.

References

1. P. Loiko, V. Dashkevich, S. Bagaev, *et al.*, "Spectroscopic characterization and pulsed laser operation of Eu^{3+}:$KGd(WO_4)_2$ crystal," Laser Phys. **23**(10), 105811 (2013).
2. P. Loiko, V. Dashkevich, S. Bagaev, *et al.*, "Spectroscopic and photoluminescence characterization of Eu^{3+}-doped monoclinic $KY(WO_4)_2$ crystal," J. Lumin. **153**, 221–226 (2014).
3. R. Jagannathan and M. Kottaisamy, "Eu^{3+} luminescence: A spectral probe in $M_5(PO_4)_3X$ apatites (M = Ca or Sr; X = F^-, Cl^-, Br^- or OH^-)," J. Phys.: Condens. Matter **7**(44), 8453–8466 (1995).
4. M. Scarafagio, A. Tallaire, K.-J. Tielrooij, *et al.*, "Ultrathin Eu- and Er-doped Y_2O_3 films with optimized optical properties for quantum technologies," J. Phys. Chem. C **123**(21), 13354–13364 (2019).
5. A. Arcangeli, M. Lovrić, B. Tumino, *et al.*, "Spectroscopy and coherence lifetime extension of hyperfine transitions in $^{151}Eu^{3+}$:Y_2SiO_5," Phys. Rev. B **89**(18), 184305 (2014).
6. C. Kränkel, D. Marzahl, F. Moglia, *et al.*, "Out of the blue: semiconductor laser pumped visible rare-earth doped lasers," Laser Photonics Rev. **10**(4), 548–568 (2016).
7. J. Park and A. Steckl, "Laser action in Eu-doped GaN thin-film cavity at room temperature," Appl. Phys. Lett. **85**(20), 4588–4590 (2004).
8. S. Bagaev, V. Dashkevich, V. Orlovich, *et al.*, "25%Eu:$KGd(WO_4)_2$ laser crystal: spectroscopy and lasing on the $^5D_0 \rightarrow {}^7F_4$ transition," Quantum Electron. **41**(3), 189–192 (2011).
9. V. Dashkevich, S. Bagayev, V. Orlovich, *et al.*, "Quasi-continuous wave and continuous wave laser operation of Eu:$KGd(WO_4)_2$ crystal on a $^5D_0 \rightarrow {}^7F_4$ transition," Laser Phys. Lett. **12**(1), 015006 (2015).
10. P. Loiko, D. Rytz, S. Schwung, *et al.*, "Watt-level europium laser at 703 nm," Opt. Lett. **46**(11), 2702–2705 (2021).

Optics EXPRESS

11. W. Carnall, P. Fields, and K. Rajnak, "Electronic energy levels of the trivalent lanthanide aquo ions. IV. Eu^{3+}," J. Chem. Phys. **49**(10), 4450–4455 (1968).
12. T. Nishida, N. Shimada, K. Ono, *et al.*, "Highly reliable 637-639 nm red high-power LDs for displays," *Proc. SPIE* 7583, 758303 (2010).
13. X. Lin, J. Liu, J. Hao, *et al.*, "Collinear holographic data storage technologies," Opto-Electron. Adv. **3**(3), 190004 (2020).
14. L. Walsh, "The current status of laser applications in dentistry," Aust. Dent. J. **48**(3), 146–155 (2003).
15. C. Dupuy, C. Hwang, D. Benenati, *et al.*, "High-power red diode laser system for photodynamic therapy," Proc. SPIE **231**, 333–341 (1994).
16. D.-R. Lee, "Progresses in implementation of STED microscopy," Meas. Sci. Technol. **34**(10), 102002 (2023).
17. C. Fan and J. Longtin, "Laser-based measurement of liquid temperature or concentration at a solid-liquid interface," Exp. Therm. Fluid Sci. **23**(1-2), 1–9 (2000).
18. A. C. Hernandez, P. A. Dominguez, O. A. Cruz, *et al.*, "Laser in agriculture," Int. Agrophys **24**(4), 407–422 (2010).
19. V. Petrov, M. Pujol, X. Mateos, *et al.*, "Growth and properties of $KLu(WO_4)_2$, and novel ytterbium and thulium lasers based on this monoclinic crystalline host," Laser Photonics Rev. **1**(2), 179–212 (2007).
20. V. Jambunathan, X. Mateos, P. Loiko, *et al.*, "Growth, spectroscopy and laser operation of Ho:$KY(WO_4)_2$," J. Lumin. **179**, 50–58 (2016).
21. J. Serres, P. Loiko, V. Jambunathan, *et al.*, "Efficient diode-pumped Er:$KLu(WO_4)_2$ laser at ~1.61 µm," Opt. Lett. **43**(2), 218–221 (2018).
22. A. Kaminskii, J. Gruber, S. Bagaev, *et al.*, "Optical spectroscopy and visible stimulated emission of Dy3+ ions in monoclinic α−KY(WO4)2 and α−KGd(WO4)2 crystals," Phys. Rev. B **65**(12), 125108 (2002).
23. A. Baillard, P. Loiko, D. Rytz, *et al.*, "Red Sm:$KGd(WO_4)_2$ laser at 649 nm," Opt. Lett. **48**(18), 4721–4724 (2023).
24. A. Baillard, P. Loiko, D. Rytz, *et al.*, "Polarized spectroscopy of Sm^{3+} ions in monoclinic $KGd(WO_4)_2$ crystals for lasers emitting in the red," J. Lumin. **273**, 120641 (2024).
25. J. Mackenzie, "Dielectric solid-state planar waveguide lasers: a review," IEEE J. Select. Topics Quantum Electron. **13**(3), 626–637 (2007).
26. E. Kifle, P. Loiko, C. Romero, *et al.*, "Watt-level ultrafast laser inscribed thulium waveguide lasers," Prog. Quantum Electron. **72**, 100266 (2020).
27. K. van Dalfsen, S. Aravazhi, C. Grivas, *et al.*, "Thulium channel waveguide laser with 1.6 W of output power and ~80% slope efficiency," Opt. Lett. **39**(15), 4380–4383 (2014).
28. D. Geskus, S. Aravazhi, E. Bernhardi, *et al.*, "Low-threshold, highly efficient Gd^{3+}, Lu^{3+} co-doped $KY(WO_4)_2$:Yb^{3+} planar waveguide lasers," Laser Phys. Lett. **6**(11), 800–805 (2009).
29. J. Carvajal, W. Bolaños, X. Mateos, *et al.*, "Tm^{3+}-based waveguide lasers in monoclinic double tungstates," J. Lumin. **133**, 262–267 (2013).
30. X. Mateos, S. Lamrini, K. Scholle, *et al.*, "Holmium thin-disk laser based on Ho:$KY(WO_4)_2$/$KY(WO_4)_2$ epitaxy with 60% slope efficiency and simplified pump geometry," Opt. Lett. **42**(17), 3490–3493 (2017).
31. V. Gorbenko, T. Zorenko, A. Kaczmarek, *et al.*, "Eu^{3+} multicenter formation and luminescent properties of $Ca_3Sc_2Si_3O_{12}$:Eu and $Ca_2YScMgSiO_{12}$:Eu single crystalline films," Opt. Mater. (Amsterdam, Neth.) **90**, 70–75 (2019).
32. N. Vasil'eva, D. Spassky, S. Omelkov, *et al.*, "Growth, optical absorption, and photoluminescence of epitaxial $(Pb,Gd)_3(Al,Ga)_5O_{12}$:Ce^{3+},Eu^{3+} films," Inorg. Mater. **58**(2), 165–171 (2022).
33. P. Tien, R. Martin, S. Blank, *et al.*, "Optical waveguides of single-crystal garnet films," Appl. Phys. Lett. **21**(5), 207–209 (1972).
34. Á. de Jesús Morales-Ramírez, M. García-Hernandez, M. Carrera-Jota, *et al.*, "Photoluminescence properties of $Lu_2Si_2O_7$:Eu^{3+} sol-gel thin films obtained using GLYMO as a silicon source," Ceram. Int. **49**(23), 38165–38173 (2023).
35. M. Scarafagio, A. Tallaire, M.-H. Chavanne, *et al.*, "Improving the luminescent properties of atomic layer deposition Eu:Y_2O_3 thin films through optimized thermal annealing," Phys. Status Solidi A **217**(8), 1900909 (2020).
36. N. Harada, A. Ferrier, D. Serrano, *et al.*, "Chemically vapor deposited Eu^{3+}:Y_2O_3 thin films as a material platform for quantum technologies," J. Appl. Phys. (Melville, NY, U. S.) **128**(5), 055304 (2020).
37. K. Ezirmik, "Concentration quenching of photoluminescence in optically transparent Lu_2O_3:Eu thin films deposited to be used as scintillators," Mater. Res. Express **8**(1), 016407 (2021).
38. S. Miranda, M. Peres, T. Monteiro, *et al.*, "Rapid thermal annealing of rare earth implanted ZnO epitaxial layers," Opt. Mater. (Amsterdam, Neth.) **33**(7), 1139–1142 (2011).
39. I. Camps, M. Borlaf, M. Colomer, *et al.*, "Structure-property relationships for Eu doped TiO_2 thin films grown by a laser assisted technique from colloidal sols," RSC Adv. **7**(60), 37643–37653 (2017).
40. S. AL-Shomar, "Synthesis and characterization of Eu^{3+} doped TiO_2 thin films deposited by spray pyrolysis technique for photocatalytic application," Mater. Res. Express **8**(2), 026402 (2021).
41. M. Novotný, M. Vondráček, E. Marešová, *et al.*, "Optical and structural properties of ZnO:Eu thin films grown by pulsed laser deposition," Appl. Surf. Sci. **476**, 271–275 (2019).
42. G.-R. Li, C.-R. Dawa, X.-H. Lu, *et al.*, "Use of additives in the electrodeposition of nanostructured Eu^{3+}/ZnO films for photoluminescent devices," Langmuir **25**(4), 2378–2384 (2009).

Optics EXPRESS

43. P. Chen, Z. Wang, S. Wang, *et al.*, "Luminescent europium-doped titania for efficiency and UV-stability enhancement of planar perovskite solar cells," Nano Energy **69**, 104392 (2020).
44. P. Loiko, P. Segonds, P. Inácio, *et al.*, "Refined orientation of the optical axes as a function of wavelength in three monoclinic double tungstate crystals $KRE(WO_4)_2$ (RE = Gd, Y or Lu)," Opt. Mater. Express **6**(9), 2984–2990 (2016).
45. R. Shannon, "Revised effective ionic radii and systematic studies of interatomic distances in halides and chalcogenides," Acta Crystallogr., Sect. A: Cryst. Phys., Diffr., Theor. Gen. Crystallogr. **32**(5), 751–767 (1976).
46. Y. Petit, S. Joly, P. Segonds, *et al.*, "Recent advances in monoclinic crystal optics," Laser Photonics Rev. **7**(6), 920–937 (2013).
47. T. Damen, S. Porto, and B. Tell, "Raman effect in zinc oxide," Phys. Rev. **142**(2), 570–574 (1966).
48. L. Macalik, P. Deren, J. Hanuza, *et al.*, "Effect of random distribution and molecular interactions on optical properties of Er^{3+} dopant in $KY(WO_4)_2$ and Ho^{3+} in $KYb(WO_4)_2$," J. Mol. Struct. **450**(1-3), 179–192 (1998).
49. L. Macalik, J. Hanuza, and A. Kaminskii, "Polarized infrared and Raman spectra of $KGd(WO_4)_2$ and their interpretation based on normal coordinate analysis," J. Raman Spectrosc. **33**(2), 92–103 (2002).
50. B. Aull and H. Jenssen, "Vibronic interactions in Nd:YAG resulting in nonreciprocity of absorption and stimulated emission cross sections," IEEE J. Quantum Electron. **18**(5), 925–930 (1982).
51. D. Findlay and R. Clay, "The measurement of internal losses in 4-level lasers," Phys. Lett. **20**(3), 277–278 (1966).
52. A. Baillard, P. Loiko, A. Pavlyuk, *et al.*, "Deep-red laser operation of cleaved single-crystal plates of $Eu:CsGd(MoO_4)_2$ molybdate," Opt. Lett. **48**(11), 2977–2980 (2023).
53. N. Chang, "Fluorescence and stimulated emission from trivalent europium in yttrium oxide," J. Appl. Phys. (Melville, NY, U. S.) **34**(12), 3500–3504 (1963).
54. E. Schimitschek, "Stimulated emission in rare-earth chelate (europium benzoylacetonate) in a capillary tube," Appl. Phys. Lett. **3**(7), 117–118 (1963).